Electronic ISSN: 1309-0267

International Journal of Engineering & Applied Sciences

IJEAS

I J E A S

Volume 14, Issue 2
2022

Published by Akdeniz University

Editorial Board

(The name listed below is not Alphabetical or any title scale)

Abstracting & Indexing

IJEAS provides unique **DOI** link to every paper published.

Editorial Scope

The journal presents its readers with broad coverage across some branches of engineering and science of the latest development and application of new solution algorithms, artificial intelligent techniques innovative numerical methods and/or solution techniques directed at the utilization of computational methods in solid and nano-scaled mechanics.

International Journal of Engineering & Applied Sciences (IJEAS) is an Open Access Journal

International Journal of Engineering & Applied Sciences (IJEAS) publish original contributions on the following topics:

Civil Engineering: numerical modelling of structures, seismic evaluation, experimental testing, construction and management, geotechnical engineering, water resources management, groundwater modelling, coastal zone modelling, offshore structures, water processes, desalination, waste-water treatment, pavement and maintenance, transport and traffic, laser scanning, and hydrographic surveying, numerical methods in solid mechanics, nanomechanic and applications, microelectromechanical systems (MEMS), vibration problems in engineering, higher order elasticity (strain gradient, couple stress, surface elasticity, nonlocal elasticity)

Electrical Engineering: artificial and machine intelligence and robotics, automatic control, bioinformatics and biomedical engineering, communications, computer engineering and networks, systems security and data encryption, electric power engineering and drives, embedded systems, Internet of Things (IoT), microwaves and optics.

Engineering Mathematics and Physics: computational and stochastic methods, optimization, nonlinear dynamics, modelling and simulation, computer science, solid state physics and electronics, computational electromagnetics, biophysics, atomic and molecular physics, thermodynamics, geophysical fluid dynamics, wave mechanics, and solid mechanics.

Mechanical Engineering: machine design, materials science, mechanics of materials, manufacturing engineering and technology, dynamics, robotics, control, industrial engineering, ergonomics, energy, combustion, heat transfer, fluids mechanics, thermodynamics, turbo machinery, aerospace research, aerodynamics, and propulsion.

CONTENTS

International Journal of Engineering & Applied Sciences (IJEAS)
Vol.14, Issue 2 (2022) 53-65
http://dx.doi.org/10.24107/ijeas.1117544
Int J Eng Appl Sci 14(2) (2022) 53-65

Numerical Investigation of Interfacial Stress Distribution in Adhesive-Bonded Joints for Different Adhesive Materials

Somnath Somadder [*], Palash Das , Md. Ashraful Islam, Md. Abdul Hasib

Department of Mechanical Engineering, Khulna University of Engineering & Technology, Khulna, Bangladesh
[*]E-mail address: somnath@me.kuet.ac.bd [*], palashdas1605002@gmail.com [b], ashraf.bitr@gmail.com [c], ahasib@me.kuet.ac.bd [d]

ORCID numbers of authors:
0000-0001-6389-234X [*],0000-0003-0137-8390, 0000-0001-8864-9645, 0000-0002-2915-7840

Received date: 18.05.2022
Accepted date: 04.08.2022

Abstract

The widespread use of adhesive bonded connections has been used in a range of technical fields. In this paper, the interfacial stress distribution of adhesive bonded joint is presented. When determining whether or not a structure is dependable for use in operation, the stresses that act along the bond line of an adhesively bonded lap joint are of the utmost importance. The purpose of this study is to develop finite element solutions that are able to anticipate shear and peel stresses using the theory of elasticity as their foundation. The effect of adhesive properties on stress distribution is investigated by using different adhesive materials. By analysing five different adhesive materials it is concluded that 'adhesive I' is more reliable for operation.

Keywords: Adhesive bonded joints, Interfacial stress, Finite element solution, Adhesive materials.

1. Introduction

The adhesive joints have found widespread application in a variety of engineering fields, in particular those fields in which proper bonding is essential to the structural integrity of the building. There are many different kinds of bonded joints, the most popular of which are the single lap joint, the double lap joint, and the scarf junction. The single lap joint is the joint that has received the most research due to its straightforward geometry and ease of preparation. The scarf joint is superior to all the other types of joints because it has the highest possible strength in the same bonding zone. The geometric discontinuity that might occur in lap joints is removed in scarf joints, which results in a reduction in the amount of stress concentration [1]. Adhesive bonded joint refers to the joint formed when two or more materials are adhered together. When two dissimilar materials are adhered together, the interface region is subjected to significant stress. On adhesively bonded joints, researchers have employed analytical, computational, and experimental methodologies. The numerical investigation of interfacial stress distribution in adhesive-bonded joints for different adhesive materials is important to select the proper adhesive for the joint. There are numerous accessible analytical models for adhesively glued joints. T. S. Methfessel and W. Becker devised a generalized model for forecasting stress distributions in thick adhesive junctions [2]. Somnath Somadder and Md. Shahidul Islam evaluated the effect of adhesive layer thickness and slant angle on piezoelectric bonded joints

by utilizing the commercial 3-D finite element software ABAQUS [3]. An analytical solution for adhesive bonded joints was proposed by Tsai et al. [4]. Mokhtari et al. conducted a computational analysis to determine the effects of material characteristics on the stress distributions in the composite double lap joint [5]. Moya-Sanz et al. built a two-dimensional numerical model in Abaqus/Standard using the cohesive zone model to study the effect of geometry on the system. It is widely acknowledged that the Moya-Sanz model is one of the most significant contributions to the field of adhesive bonded joint research [6].

Experiments on adhesively bonded joints' strength and failure loads have been carried out by a number of researchers in order to gain this information. Experiments were done in order to ascertain the failure load of a single-lap joint by Ozel et al. [7]. Fatigue analysis of fastening joints of sheet materials using finite element method was carried out by Xiaocong He et al. [8]. A new material model for 2D finite element analysis of adhesive bonded joints was developed by Libin Zhao et al. [9]. Numerical investigation of mono and bi- adhesive aluminum joints was carried out by I. Pires et al. [10]. Stress analysis of an adhesively bonded single lap joint was carried out by René Quispe Rodríguez et al. [11]. Dynamic analysis of a single lap jointed cantilever beams was investigated by Xiaocong He [12]. Mechanical behavior of adhesive joints was investigated numerically by Xiaocong He and Yue Zhang [13]. Three dimensional analysis of bi-adhesively bonded double lap joint using finite element method was investigated by H. Ozer and O. Oz [14]. An analytical model for predicting the stress distributions within single-lap adhesively bonded beams was developed by Xiaocong He and Yuqi Wang [15]. In this study the interfacial stress distribution of adhesive bonded joints for various adhesive materials have been evaluated. A numerical analysis was carried out to compare and contrast among the adhesives. ABAQUS CAE tool was used in finite element analysis.

2. Mathematical Modeling

The adherends are modeled as Bernoulli-Euler beam models with axial and bending deformation modes. The formulation of this element can be found as follows:

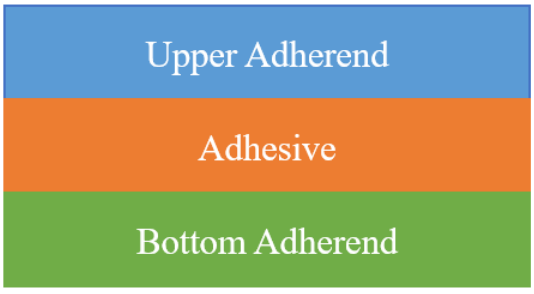

Fig. 1. General model of an adhesive bonded joint

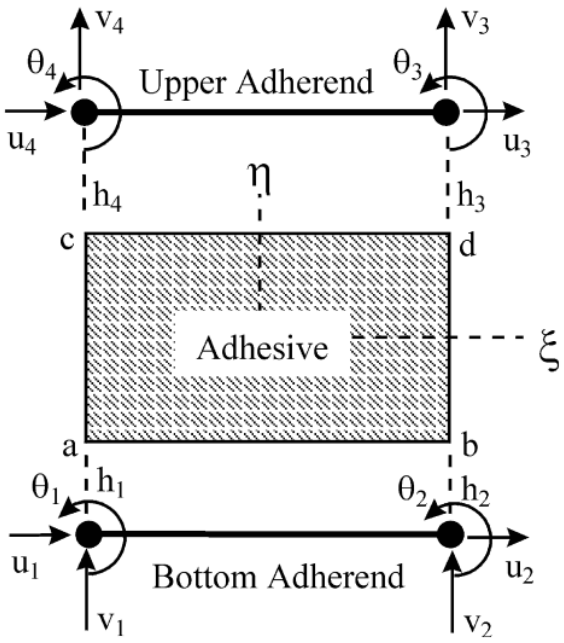

Fig. 2. 2D finite element model [16]

The axial and transverse displacement are approxiamated with the application of the following interpolation function.

$$u = \sum_{i}^{2} \psi_i u_i$$
$$v = \sum_{i}^{4} \phi_i s_i \tag{1}$$

Here, u_i and s_i are nodal displacements; ψ_i is linear Langrage interpolation function and ϕ_i is cubic Hermit interpolation function. Substituting Eq. (1) into the virtual work expression,

$$\left[K_{adher}\left(\{\Delta\}\right)\right]\{\Delta\} = \{F\} \tag{2}$$

Here, $\{\Delta\}$ is the nodal displacement vector, $K_{adher}\left(\{\Delta\}\right)$ is the stiffness matrix, $\{F\}$ is the nodal force vector.

Within the framework of the finite element discretization, the coordinates of any point within the adhesive can be described as a function of the element's nodal coordinates.

$$\{x\} = \sum N_i x_i \tag{3}$$

Here, x is the coordinate of a generic point. This leads to the following formula for the displacement of the bottom adherend,

$$\{u_{adhes}\} = \left[N_i\right]_{adhes} \{u_i\}_{adhes} \tag{4}$$

In adhesive-adherend interactions, the continuity of displacement is given by,

$$\{u_{adhes}\}_{ab} = [N_{iab}]_{adhes} \{u_i\}_{adhes} = \{u_{adher}\}_b = [N_i]_{adher} \{u_i\}_{adher_b} \tag{5}$$

$$\{u_{adhes}\}_{cd} = [N_{icd}]_{adhes} \{u_i\}_{adhes} = \{u_{adher}\}_u = [N_i]_{adher} \{u_i\}_{adher_u} \tag{6}$$

where $[N_{iab}]_{adhes}$ and $[N_{icd}]_{adhes}$ are the interpolation functions for the adhesive evaluated at the ab and cd interfaces, respectively. The displacements in the adhesive layer are derived as a function of the nodal displacement of the adherends by using these formulas.

$$\{u_{adhes}\} = [N_i^{'}]\{u\}_{adher} \tag{7}$$

where $[N_i^{'}]$ is the interpolations functions of the displacements in the adhesive layer with respect to the adherend nodal displacements.

The constitutive law of the adhesive can be expressed as,

$$D = \frac{E}{(1+\upsilon)(1-2\upsilon)} \begin{bmatrix} 1-\upsilon & \upsilon & 0 \\ \upsilon & 1-\upsilon & 0 \\ 0 & 0 & \frac{1-2\upsilon}{2} \end{bmatrix} \tag{8}$$

where E is the elastic modulus and υ the Poisson ratio

The model of the finite elements can be obtained by doing the following:

$$[K_{adhes}(\{\Delta\})]\{\Delta\} = \{F\} \tag{9}$$

The sum of the stiffness matrices of the adherend and the adhesive constitutes the model of the adherend-adhesive system.

$$[K_{adher} + K_{adhes}]\{\Delta\} = [K]\{\Delta\}\{F\} \tag{10}$$

Eq. (10) can be written as,

$$[K_L + K_{NL}]\{U\} = \{F\} \tag{11}$$

3. Finite Element Modeling

The development of the finite element model is accomplished with the help of the ABAQUS finite element program. The simulation was carried out by taking into account adhesive bonds that were stressed by mechanical loads. For the purpose of stress analysis, the general static step is utilized.

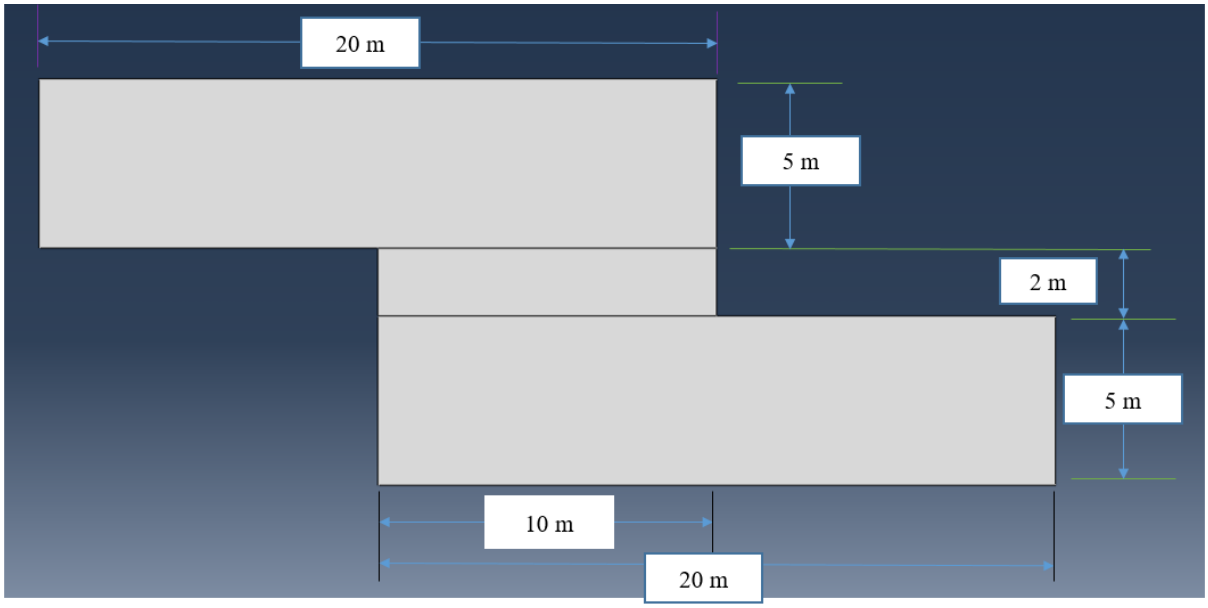

Fig. 3. Physical representation of the model

Within the scope of this study, three rectangular bars have been taken into consideration for the examination. Figure 3 shows that the upper and lower adherends each measure 20 meters in length and 5 meters across. This dimensions are taken as practical implementation of industrial applications such as electronic packaging and building constructions. The adhesive layer, which is 10 meters in length and 2 meters in width.

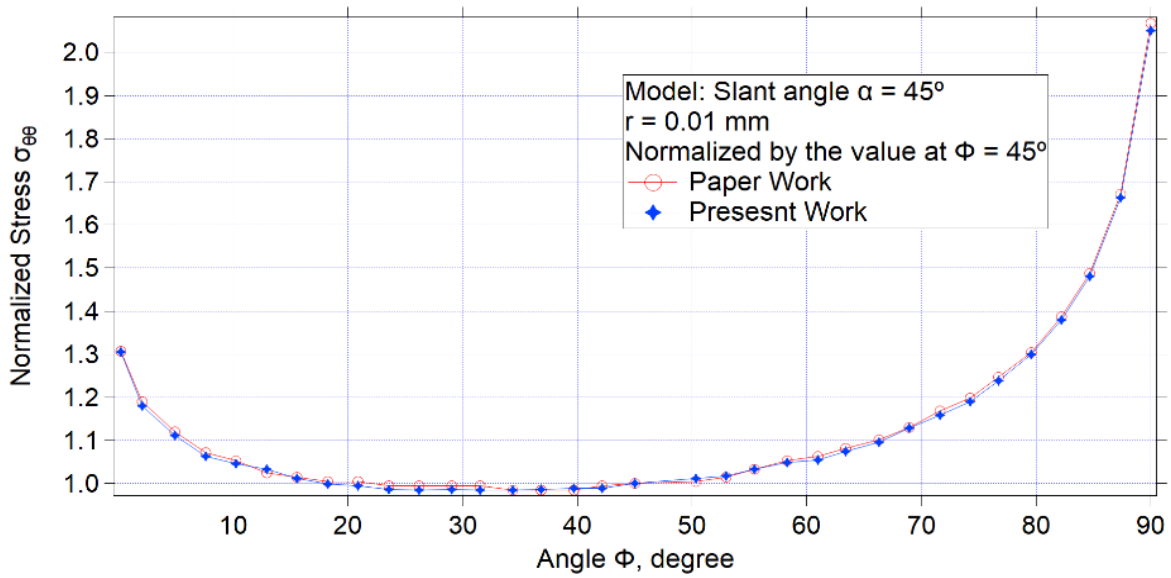

Fig. 4. Comparison of present analysis with reference paper analysis for the validation of research work

Figure 4 indicates that the results obtained in the present analysis are in good agreement with the results of Hideo Koguchi and Joviano Antonio da Costa [17] where the maximum error percentage is less than 1%.

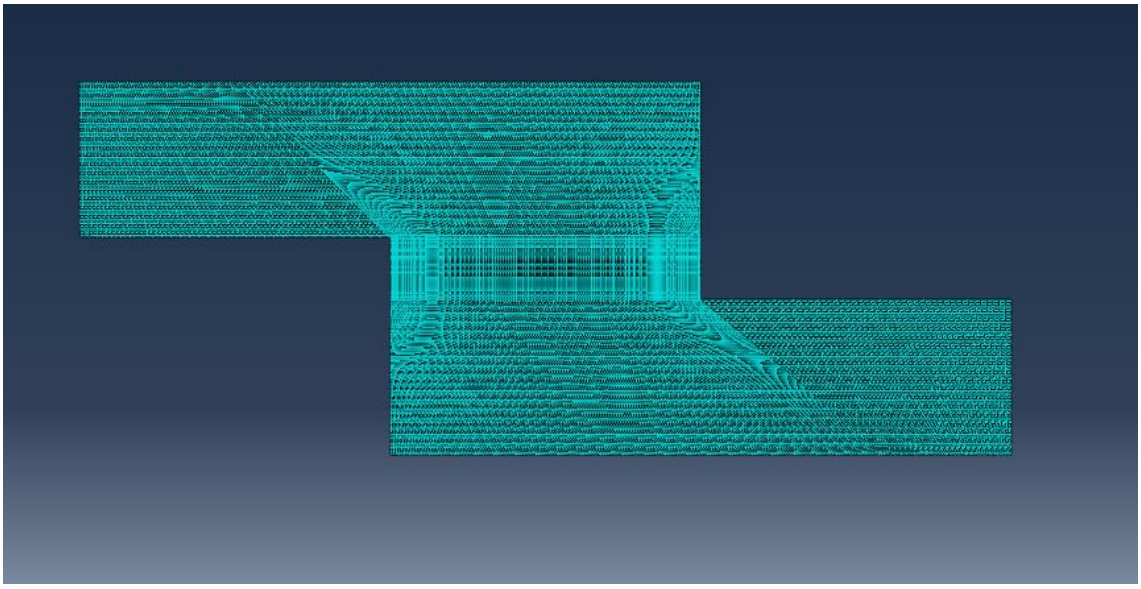

Fig. 5. Mesh of the model

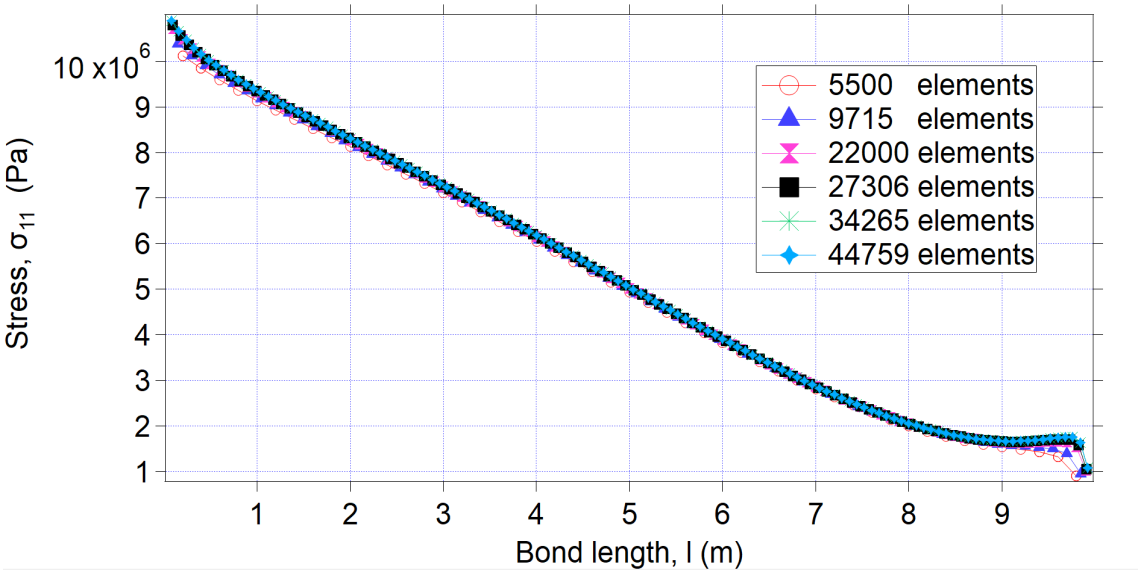

Fig. 6. Mesh sensitivity analysis of the model

Figure 5 indicates the mesh of the model. A bias has been introduced near the interface region, which has resulted in a greater concentration of elements in that region compared to those in the other regions. Because this is a two-dimensional FEM analysis, the plane stress condition is taken into account. The CPS4R mesh element type, which is a 4-node biquadratic, reduced integration element, is the one that is utilized here. Following the completion of a mesh sensitivity study as shown in figure 6, 34625 elements will be utilized in the subsequent analysis.

3.1. Material properties

Titanium is employed as the lower adherend material, and aluminum is used for the higher adherend material in this instance.

Table 1. The characteristics of the materials that were used for the examination [18].

Material	$E(GPa)$	ν
Aluminum (1050A-H9)	72	0.33
Titanium	108	0.30
Adhesive I	0.01	0.32
Adhesive II	0.1	0.33
Adhesive III	1	0.35
Adhesive IV	2	0.36
Adhesive V	5	0.40

3.2. Boundary condition

In this investigation, a mechanical force of 1 MPa is exerted on the right side of the lower adherend, while the left side of the higher adherend remains fixed. After generating the pieces and assigning material qualities the parts are joined together. The problem was effectively solved by developing a static step, putting in place appropriate boundary and loading conditions, and so on.

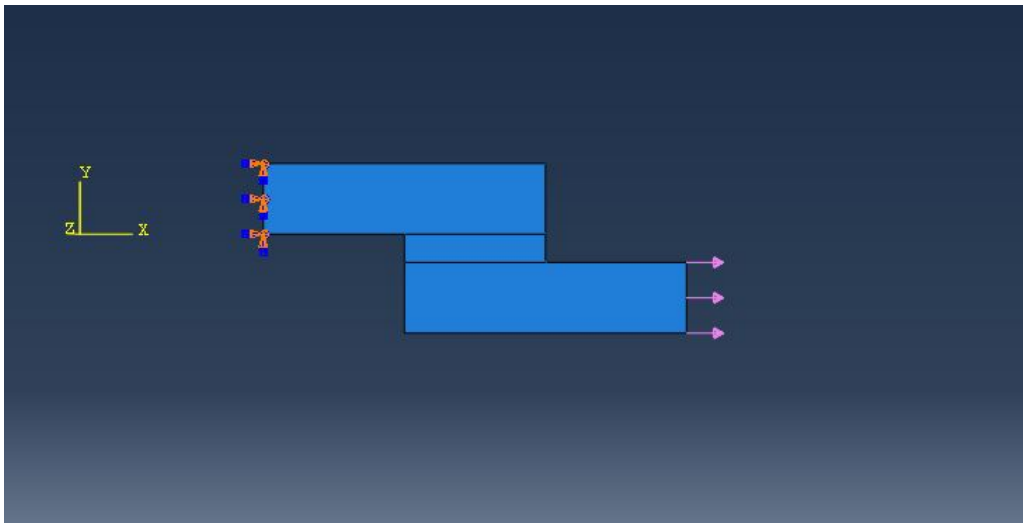

Fig. 7. Model showing boundary condition of the analysis

4. Result and Discussion

In order to analyze the stress and displacement characteristics of each simulated result, all of the results are plotted against the bond line. Please find below a presentation of the graphical illustrations.

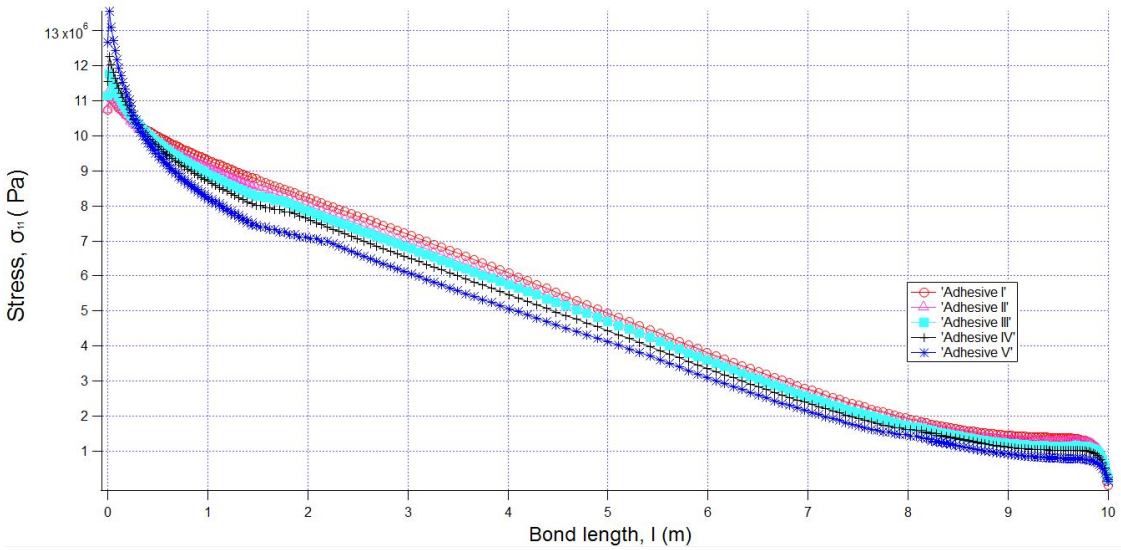

Fig. 8. Variation of σ_{11} along the bond line of the adhesive bonded joint

The distribution of σ_{11} along the bond line of the adhesive bonded joint is depicted in Figure 8. Here σ_{11} represents the variation of normal stress distribution along the X direction. It can be seen from the figure that the amount of stress is the greatest for adhesive V and that it is the lowest for adhesive I. As a result, adhesive I need to be utilized to ensure reliable operation.

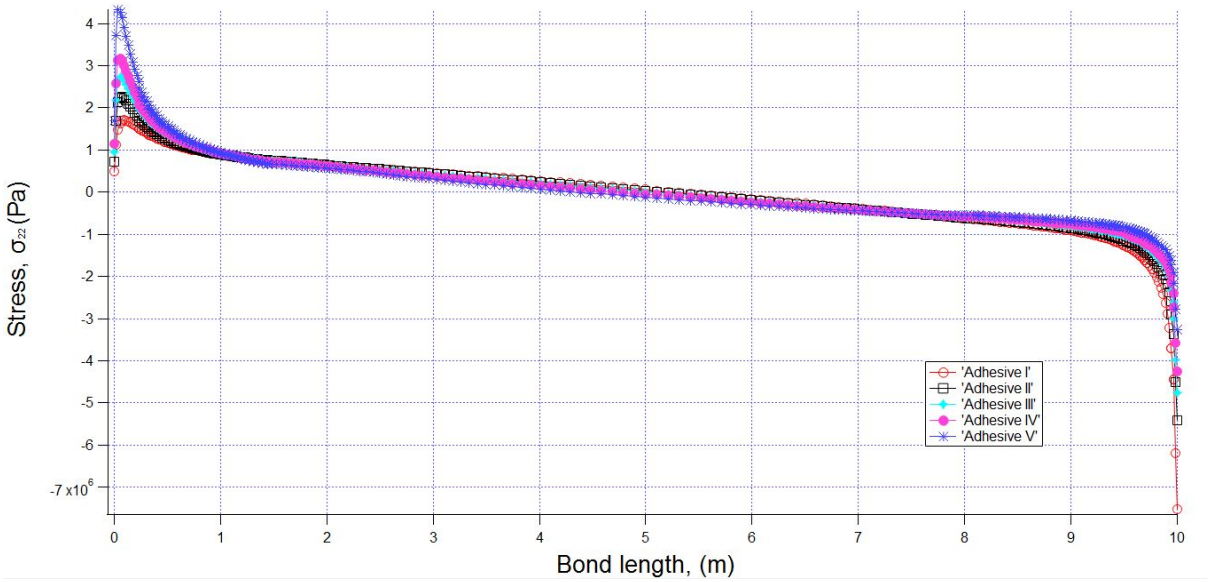

Fig. 9. Variation of σ_{22} along the bond line of the adhesive bonded joint

Figure 9 shows the distribution of σ_{22} along the bond line of the adhesive bonded joint. Here σ_{22} represents the variation of normal stress distribution along the Y direction. It can be seen from the figure that the amount of stress that is present is greater near the interface regions than it is in any of the other places. When it comes to the distribution of stress, adhesive V receives

the most while adhesive I receives the least. As a result, adhesive I should be used so that the operation can be trusted.

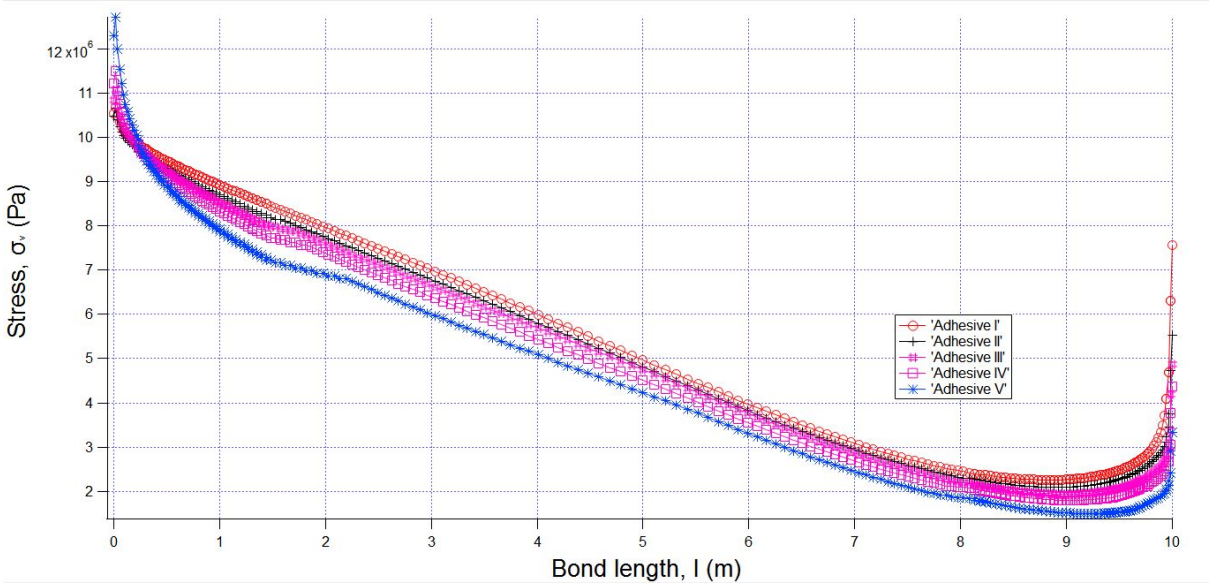

Fig. 10. Variation of Von Mises stress along the bond line of the adhesive bonded joint

The distribution of Von Mises stress along the bond line of the adhesive bonded joint is depicted in Figure 10. It can be seen from the figure that the amount of stress that is present is greater near the interface regions than it is in any of the other places. When it comes to the distribution of stress, adhesive V receives the most while adhesive I receives the least. As a result, adhesive I should be used so that the operation can be trusted.

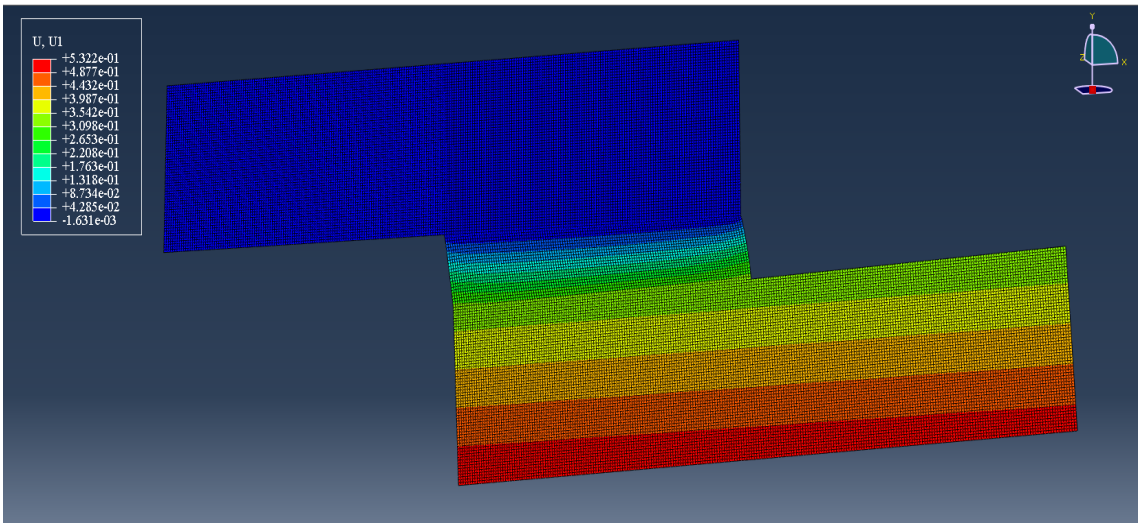

Fig. 11. Contour of displacement component u_1 for adhesive I

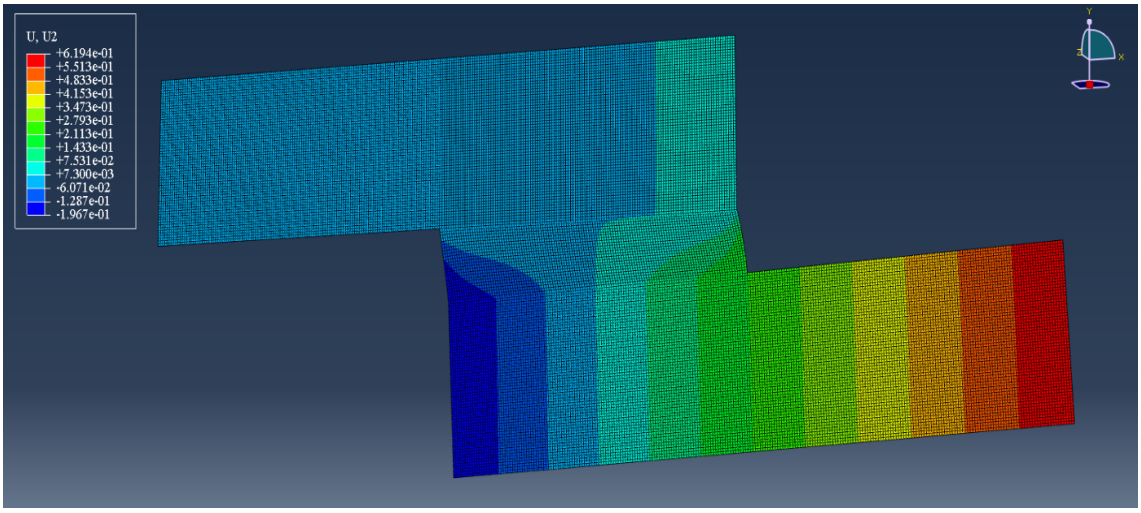

Fig. 12. Contour of displacement component u_2 for adhesive I

Figure 11 and 12 show the contour of axial and transverse displacement respectively. Maximum displacement occurs near lower adherend where the load is applied. The transverse displacement is greater than the axial displacement. Large stress and displacement occur near the edge region. Delamination and failure may occur due to large displacement and stress concentration. Therefore, selecting a proper adhesive to reduce the chance of failure is very important.

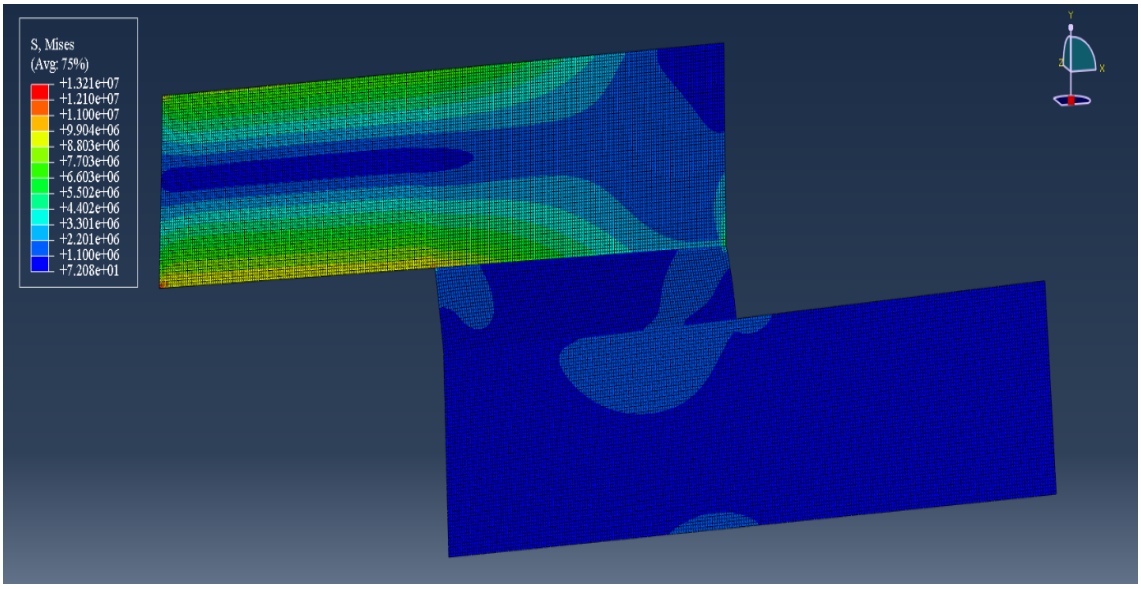

Fig. 13. Contour of Von Mises stress for adhesive I

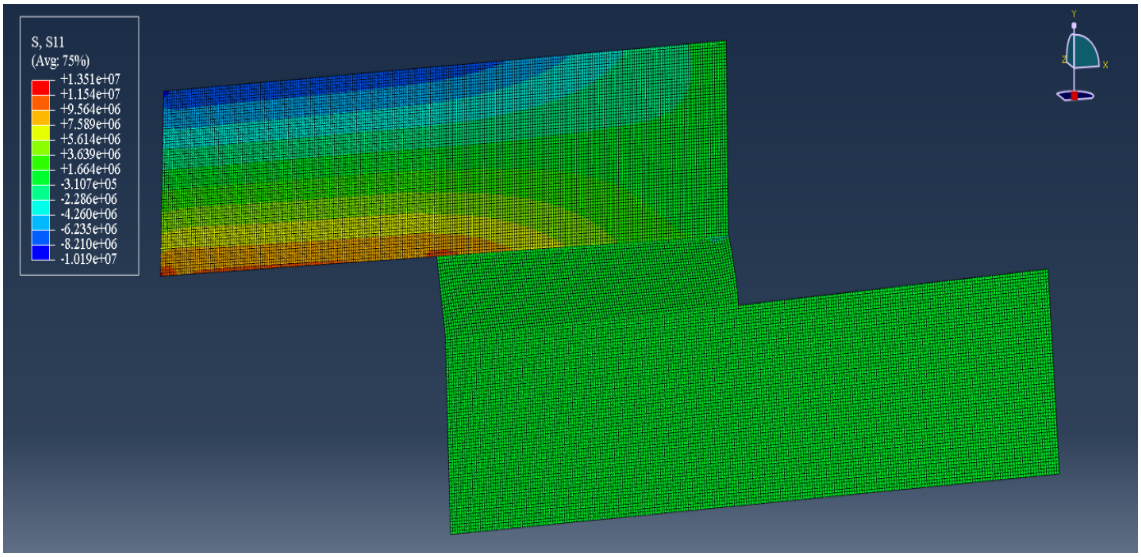

Fig. 14. Contour of stress component σ_{11} for adhesive I

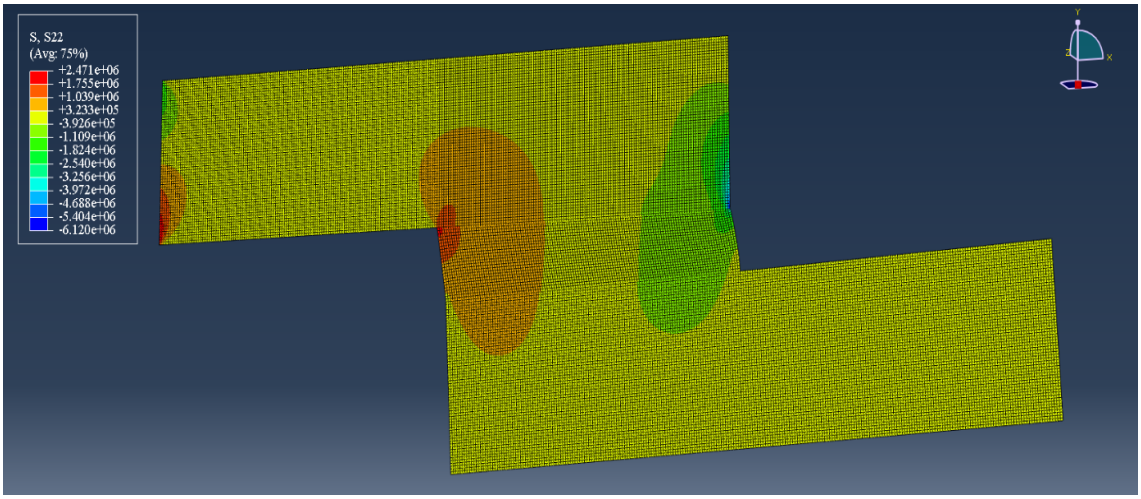

Fig. 15. Contour of displacement elements σ_{22} for adhesive I

Figure 13,14 and 15 show the contour of Von Mises stress, σ_{11} and σ_{22} respectively. Maximum stress occurs near the interface region than the other regions. Stress is found to be maximum near the edge due to the occurrence of stress singularity near the singular point. As the Modulus of elasticity and poison ratio of adhesive decreases singular stress also decrease. Due to high stress concertation delamination may occur. Therefore, selecting proper adhesive is important to reduce the chance of failure.

7. Conclusions

Using a commercial 2-D finite element code, the effect of adhesive characteristics on the interfacial stress field of adhesively bonded joints was examined. For five types of adhesive, the stress distributions along the bond length of adhesive-bonded joints are determined. The

results indicate that Young's modulus and Poisson's ratio have a significant impact on the stress and displacement fields of an adhesively bonded joint. In addition, the research reveals that the adhesive-bonded joint's strength can be increased by selecting an adequate adhesive. By analyzing five different models it can be concluded that adhesive I should be utilized for operation.

Acknowledgments

The authors would like to thank GOD for His enormous grace in allowing them to conclude their research.

Notations

u_i Nodal displacements
ψ_i Langrage interpolation function
E Young's Module
ϕ_i Hermit interpolation function
$\{\Delta\}$ Nodal displacement vector
$\{F\}$ Nodal force vector

References

[1] Liao L., Sawa T., Huang C., Numerical analysis on load-bearing capacity and damage of double scarf adhesive joints subjected to combined loadings of tension and bending. *International Journal of Adhesion and Adhesives*, 53, 65–71, 2014.

[2] Methfessel, T. S., Becker, W., A generalized model for predicting stress distributions in thick adhesive joints using a higher-order displacement approach, *Composite Structure,* 291, 2022.

[3] Somadder, S., Islam S. Md., Effect of Adhesive Layer Thickness and Slant Angle on Piezoelectric Bonded Joints, *Journal of Mechanical Engineering,* 19, 251-268, 2022.

[4] Tsai M.Y., Oplinger D.W., Morton J., Improved theoretical solutions for adhesive lap joints, *International Journal of Solids and Structures*, 35, 1163–1185, 1998.

[5] Mokhtari M., Madani K., Belhouari M., Touzain S., Feaugas X., Ratwani M., Effects of composite adherend properties on stresses in double lap bonded joints*, Materials and Design*, 44, 633–639, 2013.

[6] Moya-Sanz E.M., Ivañez I., Garcia-Castillo S.K., Effect of the geometry in the strength of single-lap adhesive joints of composite laminates under uniaxial tensile load. *International Journal of Adhesion and Adhesives,* 72, 23–29, 2017.

[7] Ozel A., Yazici B., Akpinar S., Aydin M.D., Temiz S., A study on the strength of adhesively bonded joints with different adherends, *Composites Part B: Engineering*, 62, 167–174, 2014.

[8] He X., Gu F., Ball A., Fatigue Behaviour of Fastening Joints of Sheet Materials and Finite Element Analysis, Advances in Mechanical Engineering, 5, 1-9, 2013.

[9] Zhao L., Wang Y., Qin T., Zhang J., X., A New Material Model for 2D FE Analysis of Adhesively Bonded Composite Joints, MATERIALS SCIENCE, 20, 468-473, 2014.

[10] Pires I., Quintino L., Miranda M. R., Numerical simulation of mono- and biadhesive aluminium lap joint, Advances in Mechanical Engineering, Journal of Adhesion Science and Technology,20, 19-36, 2006.

[11] Rodríguez Q. R., Sollero P., Rodrigues B. M., STRESS ANALYSIS AND FAILURE CRITERIA OF ADHESIVE BONDED SINGLE LAP JOINTS, 21st International Congress of Mechanical Engineering, 2011.

[12] He X., Dynamic Behaviour of Single Lap-Jointed Cantilevered Beams, Key Engineering Materials, 413, 733-740, 2009

[13] He X., Zhang Y., Numerical Studies on Mechanical Behavior of Adhesive Joints, Advances in Materials Science and Engineering, 2015, 1-13, 2015.

[14] Ozer H., Oz O., Three dimensional finite element analysis of bi-adhesively bonded double lap joint, International Journal of Adhesion and Adhesives, 37, 50-55, 2012.

[15] He X., Wang Y., Analytical Model for Predicting the Stress Distributions within Single-Lap Adhesively Bonded Beams, Advances in Materials Science and Engineering, 2014, 1-5, 2014.

[16] Andruet H. R., Dillard, A. D., Holzer M. S., Two- and three-dimensional geometrical nonlinear Fnite elements for analysis of adhesive joints, *International Journal of Adhesion and Adhesives*, 21, 17–34, 2001.

[17] Koguchi H., Costa D. A. J., "Analysis of the stress singular field at a vertex in 3D bonded structures having a slanted surface," International Journal of Solids and Structures, 47, 3131-3140, 2010.

[18] He X., "Effect of Mechanical Properties of Adhesives on Stress Distributions in Structural Bonded Joints" World Congress on Engineering, 2010.

International Journal of Engineering & Applied Sciences (IJEAS)
Vol.14, Issue 2 (2022) 66-76
http://dx.doi.org/10.24107/ijeas.1163134
Int J Eng Appl Sci 14(2) (2022) 66-76

Design and Analysis of a Synchronous Generator Using Finite Element Method Based ANSYS-Maxwell

Yıldırım Özüpak

Dicle University Silvan Vocational School, Electrical Department, Diyarbakır, Turkey
E-mail address: yildirim.ozupak@dicle.edu.tr

ORCID numbers of author:
0000-0001-8461-8702

Received date: 16.08.2021
Accepted date: 11.10.2021

Abstract

The most basic electrical machine that converts mechanical energy into electrical energy is synchronous machines. Synchronous machines can be operated at high speeds and low speeds for different power plants. In terms of system planning, it is important to examine the operating characteristics of the machine at idle and variable load conditions in these cycles. It is very important that generators, which are the basic components of turbines in power plants, have high efficiency when they are designed. While synchronous generators are being designed, many parameters that are compatible with each other must be arranged in an appropriate way. The efficiency of generators can vary greatly by changing very important parameters in the design. In this study, the analysis, design and analysis of the characteristic parameters of a synchronous generator are carried out with the ANSYS-Maxwell-Rmxprt integrated design and simulation program based on Finite Element Method (FEM). In this paper, parameters such as efficiency, induced voltage, phase currents and voltages and output torque of a three-phase synchronous machine were obtained depending on the electrical angle change.

Keywords: Synchronous generator, efficiency, FEM.

1. Introduction

Synchronous generators are electrical machines that are produced at different power levels from a few kVA to hundreds of MVA and are generally used for high-capacity power generation. Although their high costs seem like a disadvantage because of their large structures and capacities, their efficient work is one of their advantageous aspects. Synchronous generators, which convert the mechanical energy taken from the shaft to 1-phase or 3-phase alternating voltage, can be operated with free, special or self-excitation methods. If the synchronous generator, which consists of two basic parts, armature and inductor, is to produce low power, the armature is located in the rotating part, while the inductors of the generators that will produce high power are designed to be located in the rotating part. Since synchronous generators are generally preferred in high power generation facilities, the armature section is called the stator and the inductor section is called the rotor.

The pole structures of generators are of two different structures, cylindrical and protruding. Salient-pole synchronous generators are generally used in hydroelectric and wind power plants that require multi-pole and low speed. However, it can also be encountered in the pole structures of small power and high frequency generators [1]. The air gap distance between the stator and the rotor is one of the most important parameters for generators to produce voltages close to

pure sinusoidal, and arrangements are made in the pole structures and stator windings so that the air gap flux is sinusoidal [2].

In salient pole generators, the pole legs are usually curved. Therefore, the distance between the pole legs and the stator grooves is not the same everywhere. Thus, the flux in the air gap occurs in a sinusoidal form [3]. Since the air gap between the rotor surface and the stator surface is equal everywhere in cylindrical pole generators, sinusoidal voltages can be obtained by making shortened pitch, that is, fractional windings, in the stator windings of this type of generators. These arrangements made in the stator section also ensure that a more uniform torque is produced during the operation of the generator at the engine position. In addition, measures such as placing squirrel cage system on the rotor parts and damper windings on the pole legs, ie short-circuit bars, are also frequently encountered in the literature [4]. In synchronous generators, making the stator grooves off-axis affects the total harmonic distortion (THD) value of the obtained voltage [5]. In accordance with the international harmonic standards (IEEE-519), the voltages produced by generators below 1 kV should not exceed 5% as individual harmonic distortion and 8% for the distortion limits in the voltage waveform as THD [6]. In some cases, passive filter circuits can be designed for generator voltages within acceptable limits according to the limits of the standards. In general, the situation encountered is that there are some mechanical shapings in the pole legs, but rarely in special applications, the stator grooves are made at a certain angle from the axis. Like the asymmetrical stator winding distribution, the designs of the distributed windings also affect the generated voltage waveform [7].

Synchronous generators are widely used in systems that generate electrical energy from wind energy. Many researches are carried out around the world in the field of synchronous generator design. Different types of rotors are used in the design of the Radial Flux Permanent Magnet Synchronous Generator. The performances of these rotor types used are also different from each other. The frequently used rotor types were compared with each other using the finite element method, and the advantages and disadvantages of the induced phase voltage-phase angle relationship, the cogging moment, the flux in the air gap, and the electrical angle change efficiency relationship were revealed [8,9]. Different rotor types in high speed, high efficiency, permanent magnet synchronous generator and motor system design study; They have been evaluated in terms of their output power and in terms of creating a zig emf. Again, the output powers generated by the use of different magnetic materials used in the rotor in the engine and generator design were compared. As a result, it has been mentioned that criteria such as low cogging torque, high thermal endurance, low rotor losses, high output power per generator weight, relatively high frequency and voltage, low harmonics are required for high speed and high efficiency permanent magnet synchronous generator design [10].

Cogging moment is a very important factor in radial and axial flux permanent magnet machine design. The production difficulty and high cost of the stator of axial flux permanent magnet machines require different techniques than those used in radial flux synchronous machines to reduce the cogging moment. Cogging torque minimization techniques for axial flux synchronous machines are emphasized and alternative techniques are suggested. After the analyzes with the 3D finite element method, the results were compared with the reference engine [11].

For system planning, it is important to examine the operating characteristics of the machine in idle and variable load situations. Analytical and finite element methods were used to examine the behavior of the synchronous machine by extracting these characteristics, and parameters such as the efficiency, induced voltage, phase currents and voltages, and output torque of a three-phase synchronous machine were obtained depending on the electrical angle change.

Unlike other studies, the design of a 3000W radial flux generator is aimed in this study. The dimensions of the generator were determined in the Rmxprt environment for design and analysis. Numerical analysis of this designed generator 2D-model was done with FEM. The obtained numerical data is a preliminary design for the determination of the electromagnetic parameters of the model and the applicability of the designed model.

2. Material and Method

2.1. Mathematical model

Permanent magnet synchronous generator (PMSG) is designed to operate at a nominal 250 rpm and 50 Hz frequency. The basic mathematical Equations of PMSG are presented below [5].

$$\boldsymbol{S = 11K_{w1} * \bar{B} * Ac * \left(\frac{D}{1000}\right)^2 * \frac{L}{1000} n} \tag{1}$$

Here S is apparent power (VA), K_{w1} winding factor, $\bar{B}$ magnetic loading (T), Ac electrical loading (A/m), D stator inner diameter (m), L stator depth (m), n speed (rpm). It is important to choose the slot/pole combination with a winding factor higher than 0.866. For permanent magnet machines, magnetic loading is generally 0.45-0.8T, and electrical loading Ac can be taken in the range of 8000-30000 A/m [13]. Torque to volume ratio (TRV) in permanent magnet generators can be taken in the range of 14-42 (kN/m^3) [6].

$$\boldsymbol{TRV = \frac{T_{out}}{\frac{\pi}{4} DL}} \tag{2}$$

Where Tout is given as output torque.

$$\boldsymbol{\frac{B_g}{B_r} = \frac{1}{1+\mu_r \frac{g}{Lpm}}} \tag{3}$$

The Lpm magnet thickness can be calculated by Equation (3). Where B_g is the air gap magnetic flux density (T), B_r is the magnet flux density, g is the air gap length (m). Moreover; The leakage flux factor can be calculated from Equation (4) and Equation (5).

$$\boldsymbol{\gamma = \frac{4}{\pi}\left\{\frac{B_{so}}{2g'} \tan^{-1}\left(\frac{B_{so}}{2g'}\right) - \ln\sqrt{1+\left(\frac{B_{so}}{2g'}\right)^2}\right\}} \tag{4}$$

$$\boldsymbol{K_c = \frac{\tau_t}{\tau_t - \gamma g'}} \tag{5}$$

$$\boldsymbol{\tau_s = \frac{\pi D}{N_s}} \tag{6}$$

Where N_s represents the number of slots and τ_s represents the slot pitch (m). The phase current of the generator can be calculated as given in Eq. (7).

$$I_{ph} = \frac{P_{out}}{mV} \tag{7}$$

Where m is the number of phases and V is the rated voltage.

J_s current density (A/m^2) and conductor cross-sectional area and conductor diameter can be calculated using Equation (8) and Equation (9).

$$A_{cu,i} = \frac{I_{ph}}{J_s} \tag{8}$$

$$d_w = \sqrt{\frac{4A_{cu,i}}{\pi}} \tag{9}$$

The stator outer D_0 diameter can be calculated by Equation (10). The pole step T_{pm} is calculated by Equation (11).

$$D_0 = D + 2 * (H_{s0} + H_{s1} + H_{s2} + T_{cs}) \tag{10}$$

$$T_{pm} = W_{pm} + W_b \tag{11}$$

Where H_{s0}, H_{s1} and H_{s2} are the slot heights and T_{cs} is the stator core yoke length. Moreover; W_{pm} is the magnet width and W_b is the spacing between the poles. The efficiency of the generator is calculated as given in Eq. (12).

$$Eff = \frac{P_{out}}{P_{out}+P_{cu}+P_{core}+P_{fw}} \tag{12}$$

Where, P_{cu} denotes copper loss, P_{core} denotes iron losses in the stator and rotor, and P_{fw} denotes wind and friction losses.

2.2. Design of permanent magnet synchronous generator (PMSG)

In this section, the design stages of the permanent magnet generator analyzed with ANSYS-Maxwell-Rmxprt are given. Analytical solutions are obtained by entering the basic sizing parameters into the RMxprt module of the ANSYS MAXWELL program. As seen in Fig. 1, the appropriate machine type, basic parameters (number of poles, reference speed, friction-wind loss, inner rotor and circuit shape) are entered, basic parameters of the stator and rotor are entered. However; Some basic parameters (operation mode, rated power, operating speed and temperature, rated voltage) need to be entered into the analysis. In Maxwell 2D, the dimension to be designed for the machine geometry is selected first. According to the calculated geometry data, the machine geometry is created or automatically assigned by RMxprt. As model parameters; boundary conditions, number of turns, resistance-inductance parameters (automatically assigned by RMxprt) are given.

The size of the designed generator is given in Fig. 1. The features of the stator of the designed model are presented in Table 1, and the features of the rotor are presented in Table 2.

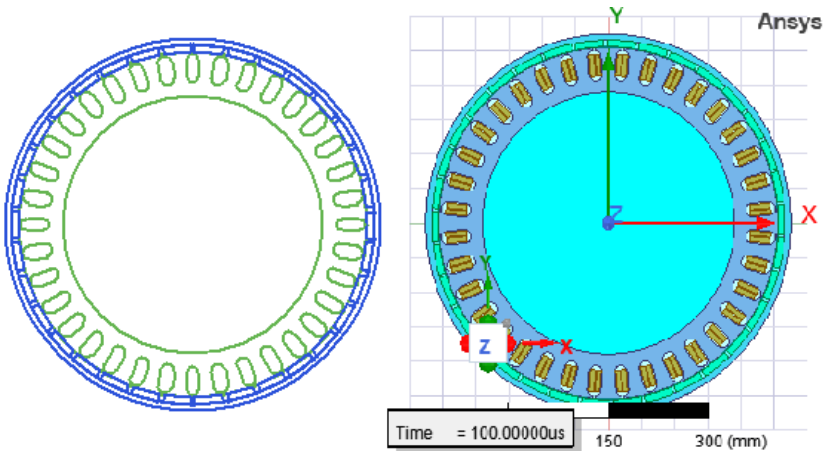

Fig. 1. ANSYS models of the designed generator

Table 1. The stator parameters of the generator model

Name	Value
"Outer Diameter"	510mm
"Inner Diameter"	380mm
Length	60mm
"Stacking Factor"	0.95
"Steel Type"	D21_50
"Number of Slots"	36
Number of conductors	24
"Slot Type"	1
Hs0	2.5mm
Hs2	25mm
Bs0	2.5mm
Bs1	20mm
Bs2	20mm

Table 2. The rotor parameters of the generator model

Name	Value
"Outer Diameter"	550mm
"Inner Diameter"	512mm
Length	60mm
"Steel Type"	D21_50
"Stacking Factor"	0.95
"Pole Type"	1
Embrace	0.9
"Magnet Type"	XG196/96
"Magnet Thickness"	10mm

In Table 3, the analysis step and output characteristics of the designed synchronous generator are listed. Losses can be seen separately through the table.

Table 3. Analysis step of the designed synchronous generator

Name	Value
"Operation Type"	Generator
"Load Type"	"Infinite Bus"
"Rated Output Power"	3000W
"Rated Voltage"	220V
"Rated Speed"	250rpm
"Operating Temperature"	75cel

3. Result and Discussion

In this part of the study, analytical and results and FEM results are presented. The graphs of the line voltage and the no-load phase voltages in the analytical calculations are given in Fig. 2. In Fig. 2, the change in phase and line voltages induced in the star connected armature according to the rotor position of the synchronous generator in the no-load condition is given. It has been determined that the total harmonic distortion in the phase and line voltages is very low in the no-load condition.

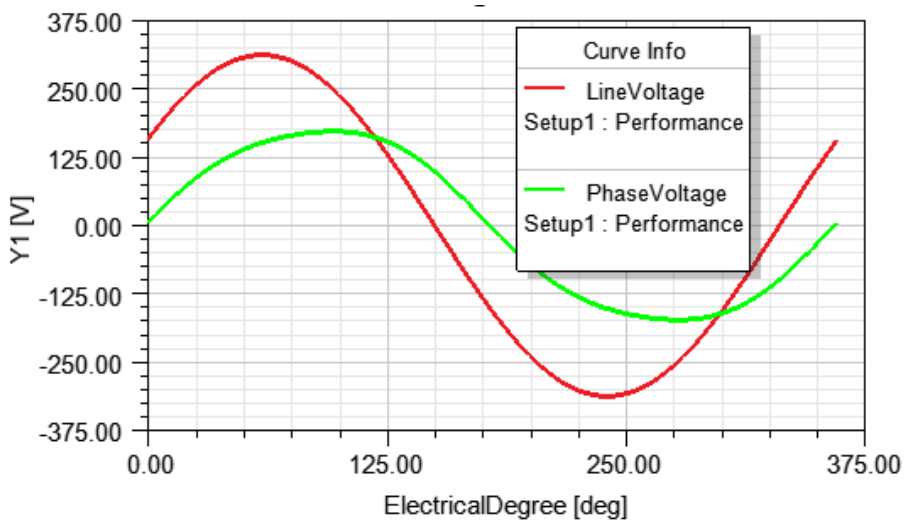

Fig. 2. No-load voltage values

In Fig. 3, the change of induced phase voltages of the synchronous generator in full load condition depending on time is given. It has been determined that the phase voltage total harmonic distortion in the full load condition is 17.84%.

In Fig. 4, the variation of the output torque of the synchronous generator with time is shown. It has been observed that the electrical output torque is at the average value of 326.4 Nm.

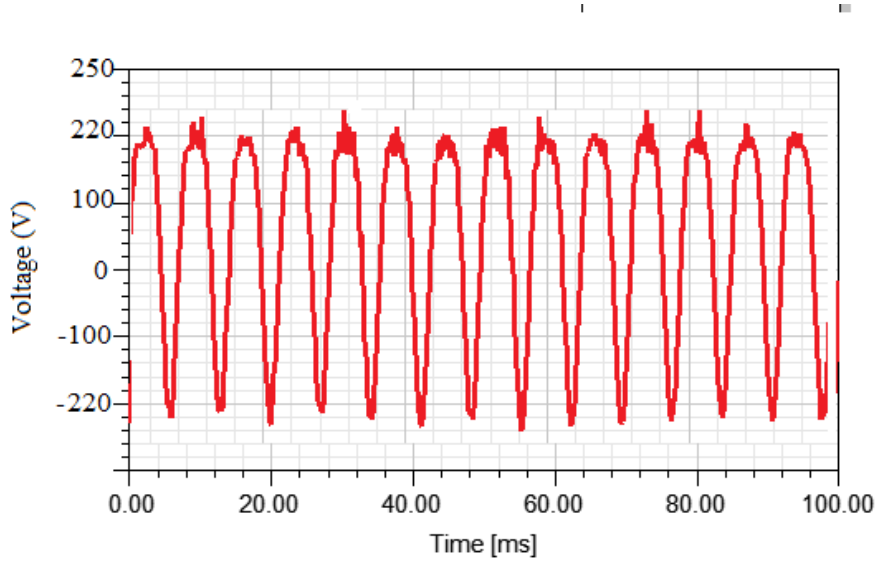

Fig. 3. Variation of induced phase voltages of synchronous generator in full load condition depending on time

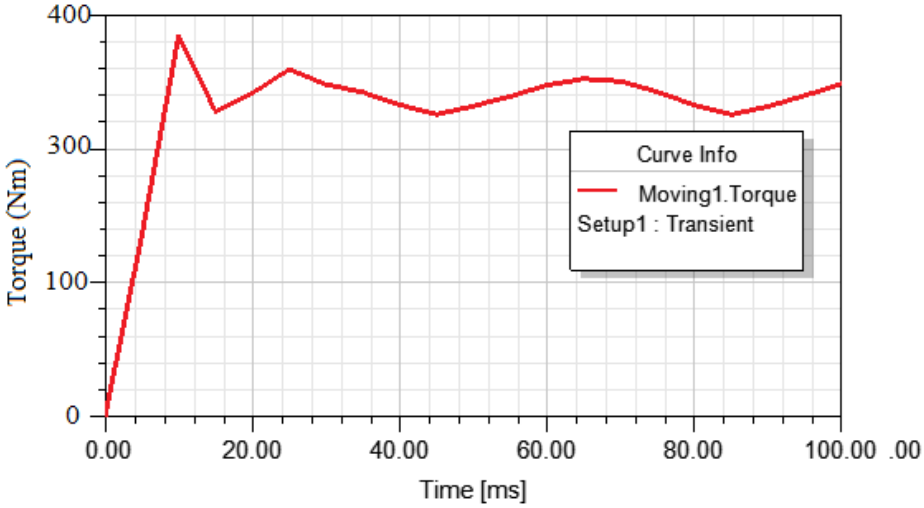

Fig. 4. Torque-time curve

In Fig. 5, the change of phase voltages depending on time is shown in the case of 0.8 back power factor of the synchronous generator analyzed according to FEM.

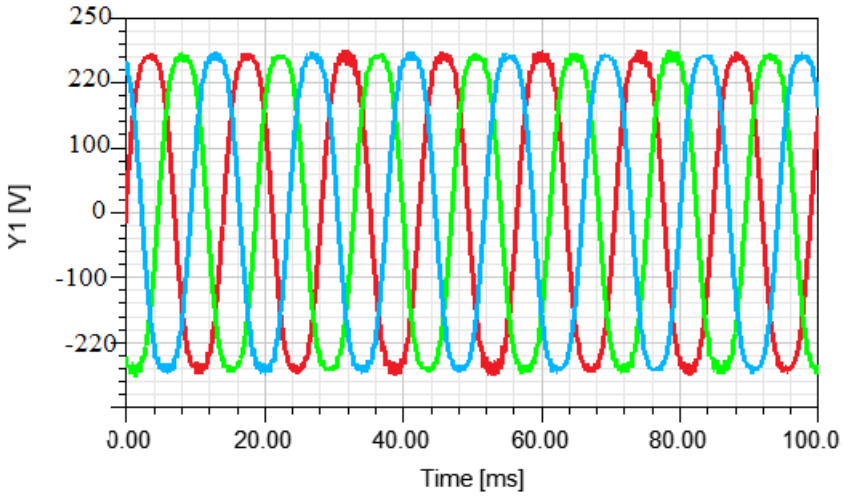

Fig. 5. Voltage-time curve

In Fig. 6, the change of phase currents depending on time is shown in the case of 0.8 reverse power factor of the synchronous generator.

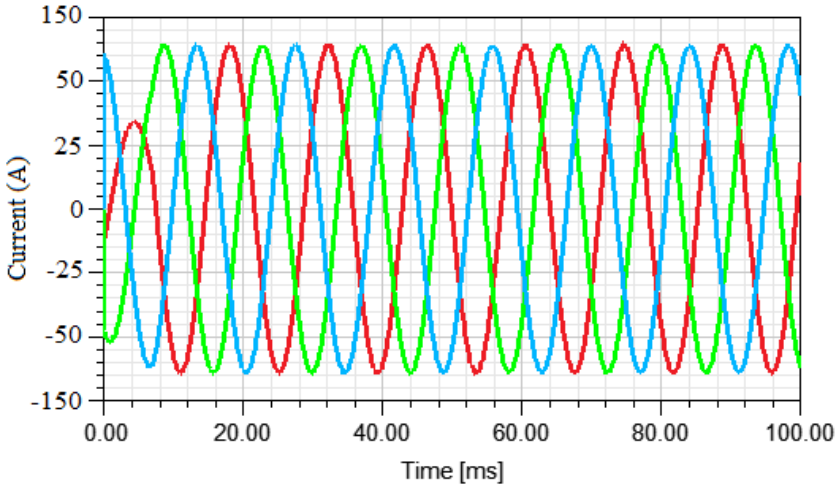

Fig. 6. Current-time graph

Fig. 7 shows the time dependent phase flux change of the synchronous generator at 0.8 back power factor.

The magnetic field intensity distribution of the designed generator model is given in Fig. 8. It is observed that the rotor saturates the magnetic material close to the windings.

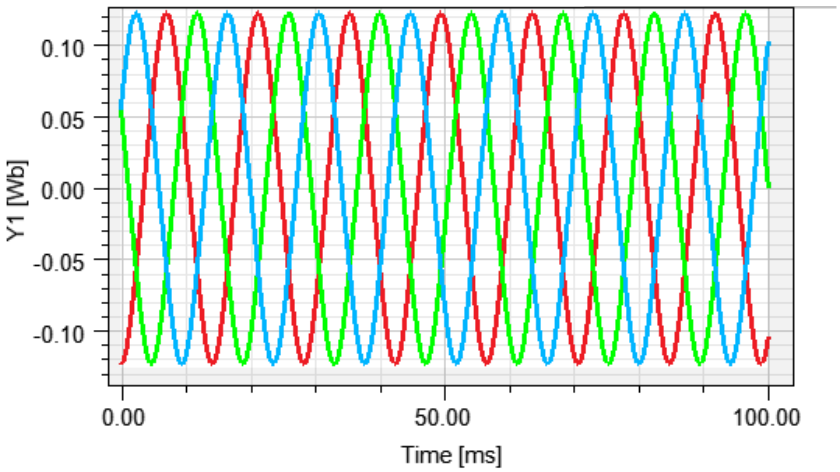

Fig. 7. Time-dependent graph of phase fluxes

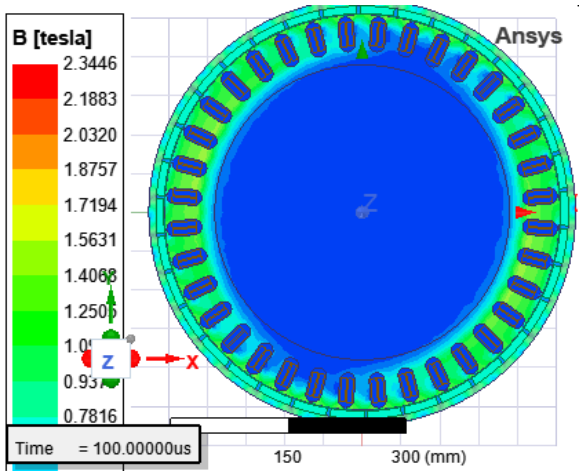

Fig. 8. Magnetic field intensity distribution of the designed generator model.

The magnetic flux line distribution of the designed generator model is given in Fig. 9. It is observed that the rotor saturates the magnetic material close to the windings.

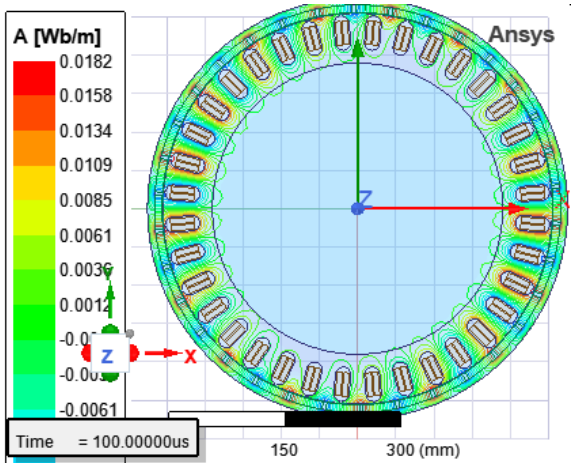

Fig. 9. Magnetic flux line distribution of the designed generator model.

The time dependent output torque variation of the synchronous generator is shown in Fig. 10. It is seen that the torque value varies in the average value of 326.4 Nm.

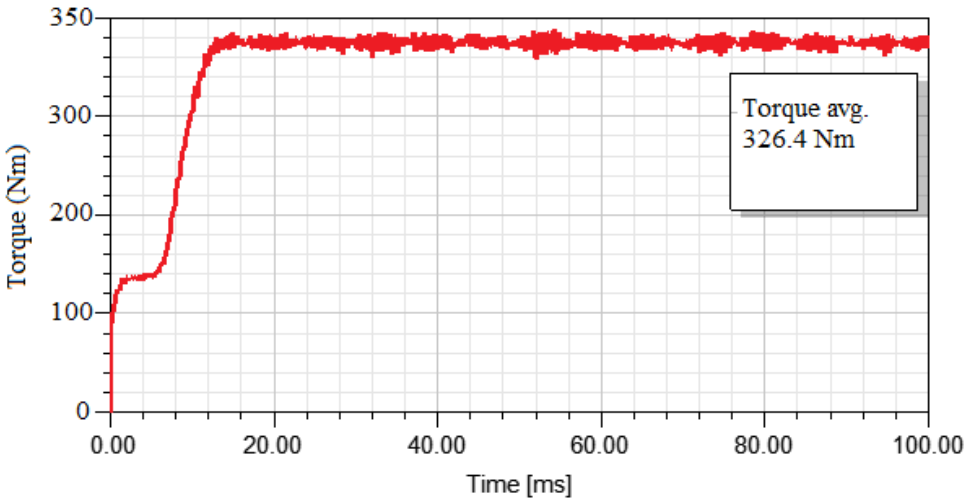

Fig. 10. Torque-time curve

4. Conclusion

In this paper, Permanent Magnet Synchronous Generator has been designed. Parametric analyzes were made in the RMxprt environment of the design. The efficiency of the designed synchronous generator, the induced voltage at the determined revolutions, the phase currents and phase voltages, the amount of torque are obtained depending on the electrical angle and time change. In addition, the magnetic flux distribution and magnetic field lines of the generator were determined by FEM, which is a numerical analysis method in ANSYS-Maxwell environment. The weak and strong points of the generator simulator, which was designed and analyzed in this integrated simulation environment, were determined. If a prototype generator model is to be developed based on this simulation model, it is necessary to pay attention to the flux density values at these points in order to prevent magnetic saturation in the core and yoke.

Acknowledgments

This study was supported by Dicle University Scientific Research Unit. Project number. SMYO-220001.

References

[1] D. D. Hanselman, Brushless Permanent Magnet Motor Design, Orono: Electrical and Computer Motorering University of Maine, ISBN 1-881855-15-5, 2003.

[2] P. M. Dusane, Simulation of a Brushless DC Motor in ANSYS- Maxwell 3D, MSc. Thesis, Czech Technical University in Prague, 2016.

[3] L. J. Young, G. H. Lee, J. P. Hong and J. Hur, Comparative study of line start permanent magnet, skeleton type brushless and Snail cam type switched reluctance motor for a fan, Sixth International Conference on Electrical Machines and Systems, ICEMS, 1, 183- 186, 2003.

[4] N. Shrivastava, A. Brahmin, Design of 3-Phase BLDC Motor for Electric Vehicle Application by Using Finite Element Simulation, International Journal of Emerging Technology and Advanced Motorering, 4(1), 2014.

[5] S. Williamson, T.J Flack, Volschenk A.F. Representation of skew in time-stepped two-dimensional finite-element models of electrical machines, IEEE Transactions on Industry Applications, 31 (5), 1009-1015, 1995.

[6] IEEE-SA Standards Board. IEEE Recommended Practice and Requirements for Harmonic Control in Electric Power Systems. IEEE Power and Energy Society, IEEE Std 519™-2014.

[7] T. Waghmare, P.R. Choube, Design Of Internal Permanent Magnet Brushless Dc Motor Using Ansys, International Journal Of Research Publications In Motorering And Technology, ISSN: 2454-7875, 2(4), 2016.

[8] A. Mujianto, M. Nizam, Comparation of the slot less brushless DC motor (BLDC) and slotted BLDC using 2D modeling, IEEE Int. Conf. On Elec Eng and Comp Sci (ICEECS), DOI:10.1109/ICEECS.2014

[9] M. Ouada, M.S Meridjet, M S. Saoud and N. Talbi, Increase Efficiency of Photovoltaic Pumping System Based BLDC Motor Using Fuzzy Logic MPPT Control, WSEAS Transactions on Power Systems, 8(3), 2013.

[10] Y. Li, T. A. Walls, J.D. Loyd, and J. L. Skinner, A noveltwo- phase BPM drive system with high power density and lowcost, IEEE Transaction On Industry Applications, 34(5), 1072- 1080, 1998.

[11] M. Sameeullah and S. Chandel, Design and Analysis of Solar Electric Rickshaw: A Green Transport Model, IEEE, 2016

[12] Ansys Electronics Desktop. R1 Rmxprt Help Datasheets, 2022